Acoustic radiation from a fluid-filled, subsurface vascular tube with internal turbulent flow due to a constriction

Yigit Yazicioglu, Thomas J. Royston,[a] Todd Spohnholtz, Bryn Martin, and Francis Loth
Mechanical Engineering, University of Illinois at Chicago, 842 West Taylor Street, MC 251, Chicago, Illinois 60607-7022

Hisham S. Bassiouny
Surgery, Section of Vascular Surgery, University of Chicago 5841 South Maryland Avenue, MC 5028, Chicago, Illinois, 60637

(Received 18 February 2005; revised 17 May 2005; accepted 24 May 2005)

The vibration of a thin-walled cylindrical, compliant viscoelastic tube with internal turbulent flow due to an axisymmetric constriction is studied theoretically and experimentally. Vibration of the tube is considered with internal fluid coupling only, and with coupling to internal-flowing fluid and external stagnant fluid or external tissue-like viscoelastic material. The theoretical analysis includes the adaptation of a model for turbulence in the internal fluid and its vibratory excitation of and interaction with the tube wall and surrounding viscoelastic medium. Analytical predictions are compared with experimental measurements conducted on a flow model system using laser Doppler vibrometry to measure tube vibration and the vibration of the surrounding viscoelastic medium. Fluid pressure within the tube was measured with miniature hydrophones. Discrepancies between theory and experiment, as well as the coupled nature of the fluid–structure interaction, are described. This study is relevant to and may lead to further insight into the patency and mechanisms of vascular failure, as well as diagnostic techniques utilizing noninvasive acoustic measurements. © *2005 Acoustical Society of America.* [DOI: 10.1121/1.1953267]

PACS number(s): 43.80.Qf, 43.40.Rj, 43.40.Ey, 43.20.Mv [FD] Pages: 1193–1209

I. INTRODUCTION

Physician-based stethoscopic auscultation of blood vessels has long been used as a simple noninvasive means of *qualitatively* assessing their patency. Increased audible frequency (sonic) sounds are associated with constrictions or other geometric alterations in the vessel geometry. These can be a result of plaque build-up in arteries, such as the coronary or common carotid, which may lead to a localized loss of circulation. A constriction can also result from intimal thickening, which commonly occurs near arteriovenous (AV) grafts that are used for dialysis patients. In recent years there has been growing interest in the correlation of sonic phenomena with vascular pathology from two perspectives, mechanistic and diagnostic.

First, from a mechanistic point of view, it is believed that identifying the cause and effect relationships between sonic phenomena and other symptoms associated with vascular pathology could lead to improved surgical practices or treatments. For example, consider AV grafts and venous anastomotic intimal hyperplasia (VAIH). Individuals with end-stage renal disease would die within a few weeks or months if not sustained by some form of dialysis therapy or a kidney transplant. An AV graft is constructed by the joining of an artery to a vein to provide an access site for hemodialysis patients. By bypassing the high resistance vessels (arterioles and capillaries), high flow rates can be achieved that are necessary for efficient hemodialysis. A synthetic graft material, polytetrafluoro-ethylene (PTFE), is often used for these grafts. More than half of the AV grafts fail and require surgical reconstruction within 3 years.[1] The majority of these graft failures is caused by occlusive VAIH, which is characterized by a narrowing or stenosis of the vein downstream of the graft junction. While the natural healing response after surgery causes some degree of intimal thickening, the biomechanical environment appears to be responsible for progression of intimal thickening to occlusive VAIH. Biomechanical forces in the AV graft are unique, with generally high wall shear stress (WSS) acting on the vein, flow separation, and significant pressure fluctuations that vibrate the vein wall and surrounding tissue. Studies in a canine animal model have shown that perivascular tissue vibration is correlated with VAIH ($r=0.92, p<0.001$).[2] Vibration likely occurs as a result of the transitional and turbulent flow patterns that exist in the AV graft due to the high flow rate and complex geometry.[3,4] An obvious question is whether this vibration has helped to catalyze or accelerate VAIH, or is it merely a benign symptom. If it is the former, then perhaps a modified graft geometry or construction should be considered in order to minimize this vibration.

Second, from a diagnostic viewpoint, whether or not turbulence-induced tissue vibration is an exacerbating catalyst of pathology or merely a benign by-product, its existence affords its use as a diagnostic indicator. To have quantitative utility and to be independent of individual physician skill and experience, a more rigorous analysis of the sonic phenomena is needed than can be obtained via the human ear and stethoscopic auscultation. In this context, there have

[a]Electronic mail: troyston@uic.edu

been numerous studies reported in the literature for more than three decades that have empirically and stochastically correlated sonic acoustic "signatures" with associated pathology.[5–17] A common observation in these studies is that sound intensity tends to increase with stenosis severity (until occlusion becomes nearly total), especially at audible frequencies on the order of hundreds of hertz (~100 to 1000 Hz), and that this sound is associated with turbulence in the stenosed vessel distal to the constriction. Some have sought to put this into a diagnostic "imaging" format via use of a two-dimensional array of acoustic transducers mounted on the skin surface that can be used to passively beamform on the sonic source.[18,19] Others have shown that the Doppler mode of conventional ultrasound (US) imaging technology can be used to roughly quantify the level of tissue vibration associated with VAIH in AV grafts.[2] Similarly, another study reported the development of an ultrasonic pulse–echo multigate technique using quadrature phase demodulation to obtain simultaneous measures of tissue vibration and blood velocity at multiple depths, again showing correlation in a case study of a severe stenosis in a human infrainguinal vein by-pass graft.[20]

A barrier to further refinement of diagnostic techniques or improved mechanistic comprehension is the limited understanding of the complex and coupled transitional or turbulent fluid and structural dynamics of the constricted blood vessel embedded in viscoelastic soft tissue layers. Numerous empirical and semiempirical models have been proposed to correlate measurements of the turbulent pressure field downstream of the occlusion with the geometry of the occluded vessel and the flow rate.[5,8–12,16] Note that, even for relatively simple geometries, an exact solution using computational fluid dynamic (CFD) simulations is as of yet unavailable for the case of transitional fluid behavior and compliant vessel wall dynamics. Accurate CFD simulations for transitional flow problems with anatomically correct, yet assumed rigid vessel walls require substantial CPU time and are just now being reported.[3,4]

Other studies have attempted to model the relationship between the turbulent field and resulting vessel vibration.[6,12,21] These studies have essentially noted that the tube-wall vibration spectra can differ significantly from the turbulence spectra as a result of the tube's frequency-dependent mobility. Additionally, it still remains somewhat unclear as to which scenario is more prevalent: (1) broad turbulence generates wall vibrations with some resonant spectral content that may subsequently cause coherent oscillations in the blood flow; or (2) coherent vortex shedding of the blood flow causes wall vibrations with distinct spectral content.[20] Still others have then tried to predict measurements by surface sensors, accounting for intervening tissue layers.[16,18] In addition to axisymmetry of the blood vessel and constriction, Ref. 16 assumed that the surrounding soft tissue is also axisymmetrically arranged about the vessel. The surrounding tissue is then treated as another fluid medium, only supporting compression waves, not shear or surface waves. On the other hand, Ref. 18 only considered shear wave radiation in the soft tissue from the turbulent source, assigning general attenuation rates to it based on geometric spreading and material viscosity.

Almost absent from the literature is a closed-form theoretical model of the entire coupled fluid/structure problem, starting from the generation of turbulence, the corresponding vessel wall vibration, and resulting surrounding tissue vibration. As noted above, a few studies have attempted this, but with the indicated limiting assumptions.[16,18] The present article reviews a theoretical and experimental study that endeavors to improve the fundamental understanding of this complex, coupled problem by considering a simple, axisymmetric, constricted vascular phantom model, in terms of its individual components as well as the assembled, coupled system. Laser Doppler vibrometry and miniature catheter hydrophone measurements provide an extensive experimental quantification of the fluid and structural behavior. While the theoretical model for fluid turbulence must be empirical, given the current state of the art, the remainder of the closed-form analytical model is based on first principles. Low-amplitude displacements of the vessel wall and surrounding tissue are assumed, which enables a linear treatment of the solid tissue dynamics. While this assumption should enable one to capture much of the dynamic phenomena present *in vivo* and in the *in vitro* phantom model described in this article, it is acknowledged that some documented phenomena will not be predicted. For example, flexible tube collapse, or buckling, after a stenosis due to the lowered intraluminal pressure has been reported *in vivo* and carefully studied *in vitro*. It can occur under both laminar and turbulent flow conditions. This involves large deformation of the lumen and requires nonlinear analysis, and is not within the scope of this article. See Ref. 22 for a review of this topic and its biological applications.

In the present article, experiments and theoretical developments are reviewed that attempt to quantify the fluid environment, its coupling to the vessel wall, and the resulting sound radiation into media exterior to the vessel wall. It is emphasized that the focus here is on developing a closed-form analytical model that may yield unique insight. Consequently, this article is divided into the following sections:

(1) description of the constricted flow phantom model and experimental measurement methods;
(2) adaptation and experimental evaluation of an empirical model for fluid turbulence;
(3) development and experimental evaluation of a theoretical model for fluid–vessel coupling; and
(4) development and experimental evaluation of a theoretical model for radiation into surrounding fluid or viscoelastic medium, including measurement of the sonic phenomena on the surface of a viscoelastic medium within which the constricted vessel is embedded.

II. THE AXISYMMETRIC CONSTRICTED FLOW MODEL

A. The experimental model

A simple axisymmetric tube geometry and flow constriction is considered. The compliant fluid-filled latex tube (Latex Penrose Tubing, Sherwood Medical, St. Louis, MO) is

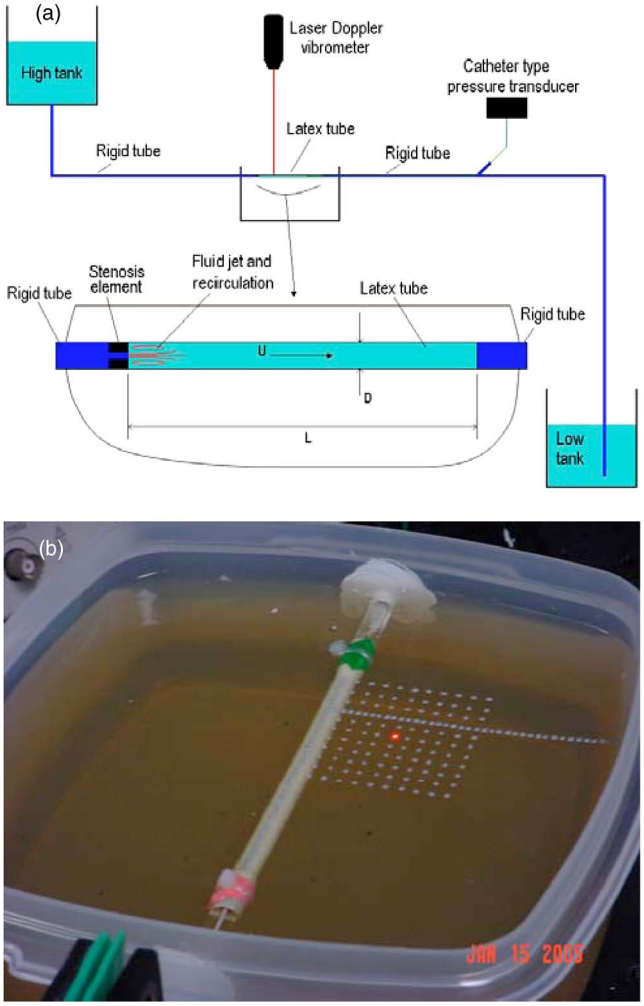

FIG. 1. (Color online) Experimental system. (a) Schematic. (b) Photograph of compliant tube embedded in gel phantom. Retroreflective tape visible on gel surface.

externally unconstrained (except at its ends) or lies just below and parallel to the horizontal free surface of a water-filled container or gel phantom model, as indicated in Fig. 1. Approximately 5% axial strain is imposed on the latex tube in all cases to prevent sagging in the externally unconstrained case. The experimental model geometry and parameter values are provided in Fig. 1 and Table I. Gravity-fed flow rates producing Reynold's (Re) numbers sufficient for turbulent generation downstream of the constriction and within the regime of biological relevance are considered. By adjusting the height of the upper water reservoir and adjusting a valve downstream of the compliant tube section, the flow rate and mean pressure within the compliant tube section are independently controlled. Degassed water is used. Steady flow rate conditions are used, as the frequency band of dynamic response associated with turbulent behavior is above and well separated from low-frequency dynamics associated with the pulsatile nature of blood flow *in vivo*.[11]

B. Experimental measurement methods

Mean and dynamic pressure within the tube, tube radial wall velocity, and gel phantom vertical velocity (when present) were measured for various flow conditions. Pressure measurements were made using a catheter-type pressure transducer (SPR-524, Millar, Houston, TX), with a bandwidth of ~10 kHz according to the manufacturer. The pressure transducer had a 1.08-mm-diameter tip where the active element was located at the end of a 0.71-mm-diameter wire. The tip was fed into the flow system from the downstream side through a sealed connector. The pressure measurements were made in 2.5-mm increments from 2.5 to 100 mm downstream of the constriction. The radial position within the tube of the catheter tip was consistently closer to the tube wall than the tube axis.

A noncontacting laser Doppler vibrometer (LDV) (CLV 800-FF/1000, Polytec, Auburn, MA) with threshold sensitivity of ~1 μm/s, low-pass filtered at 5 kHz, was used to measure tube and phantom surface velocity. Small pieces of adhesive retroreflective tape (3*M*, St. Paul, MN) measuring $\sim 1 \times 1$ mm were placed on the tube and phantom surface to improve the LDV signal. When used on the tube surface, reflective tape pieces were spaced 2.5 mm apart along the flow direction of the 100-mm tube, resulting in 41 data points (coinciding with internal pressure measurement points). On the phantom surface, they were spaced in 2.5 -mm increments along the tube axis and 2.5- or 5-mm increments lateral to it [see Fig. 1(b)]. Tube radial velocity was also measured in some cases when the tube itself was submerged in water or buried in the tissue-mimicking phantom. This measurement was more challenging because of the partial scattering of laser light at the water and phantom surfaces, which were in motion due to the turbulence-generated vibration; measurements through the phantom material during the higher flow rate case were not possible.

A two-channel digital dynamic signal analyzer (35670a, Agilent, Palo Alto, CA) was used to capture the experimental data. The acquired signals were processed using the signal

TABLE I. Experimental system parameter values.

Parameter	Value
Inner diameter of flexible tube (D)	6.4 mm
Diameter of constricted zone (d)	2.3 mm
Length of flexible tube (L)	100 mm
Wall thickness of flexible tube (h)	0.3 mm
Distance from gel or water surface to top of latex tube (h_g)	6.5 mm
Density of latex tube material (ρ_L)	1086 kg/m^3
Young's modulus for latex tube material[a] (E_L)	800 kPa
Linear viscous loss factor for latex tube material[b] (χ)	2×10^{-4} s
Poisson's ratio for latex tube material[a] (υ)	0.495
Water density[c] (ρ_f)	1000 kg/m^3
Speed of sound in water[c] (C_f)	1490 m/s
Phantom gel density (Ref. 31) (ρ_e)	1000 kg/m^3
Phantom gel volume elasticity (Ref. 31) (λ_1)	2.6 GPa
Phantom gel shear elasticity (Ref. 31) (μ_1)	4.5 kPa
Phantom gel shear viscosity (Ref. 31) (μ_2)	4 Pa s

[a]Based on quasistatic measurements in lab.
[b]Based on comparing theoretical predictions to experimental results in Figs. 6 and 7.
[c]Values based on nominal room temperature of 21 °C at atmospheric pressure.

TABLE II. A tabular approximation of $F_{n1}[x/D]$ based on Fig. 12 of Tobin and Chang (Ref. 9).

x/D	0	1	1.5	2	2.5	3	4	6	8	10	15	70
$F_{n1}[x/D]$	0	0.02	0.03	0.0355	0.0355	0.025	0.01	0.004	0.003	0.0025	0.002	0.002

analyzer and postprocessed with MATLAB V7.0. Time data were acquired at a 4096-Hz sample rate with the corresponding 120-dB/decade antialias filter set at 1600 Hz. The auto power spectra of 64 independent time records were averaged for each measurement point for each case.

III. AXISYMMETRIC FLOW CONSTRICTION AND TURBULENT FLOW

A. Theory based on empirical analysis of compliant wall studies

As noted in the Introduction, there have been numerous studies of flow in cylindrical channels with axisymmetric constrictions that are similar to the one depicted in Fig. 1(a) Researchers have theoretically, computationally, and experimentally analyzed the turbulent flow field in both relatively rigid and compliant tubes. Results and derivations reported in several specific articles were found to be most useful for the present analysis.[9,18,23]

Given the axisymmetric tube and constriction, it is assumed that the pressure distribution on the inner tube wall is also axisymmetric. The dynamic (acoustic) pressure $p(x,t)$ is only dependent on one spatial variable, the axial location x along the tube, as well as time, t. Its dependence on time and its dependence on x, are random, but with underlying time-averaged trends.[23] The turbulent coherent structures that produce dynamic pressure variations are assumed to propagate down the tube at a mean speed equal to the steady-state flow speed, but with significant random variation in the speed. Consequently, while $p(x,t)$ is random, a deterministic spectral approximation may be reasonable. A deterministic expression for $p(x,f)$, where f is the cyclic frequency in hertz (Hz), will be developed based on the literature.

Tobin and Chang[9] studied steady flow of water in a straight, compliant (latex rubber) cylindrical tube of diameter $D=7.94$ mm with a constricted region of various diameters d. The latex tube rested horizontally on 100 mm of cotton batting to isolate it from building vibrations. The tube itself

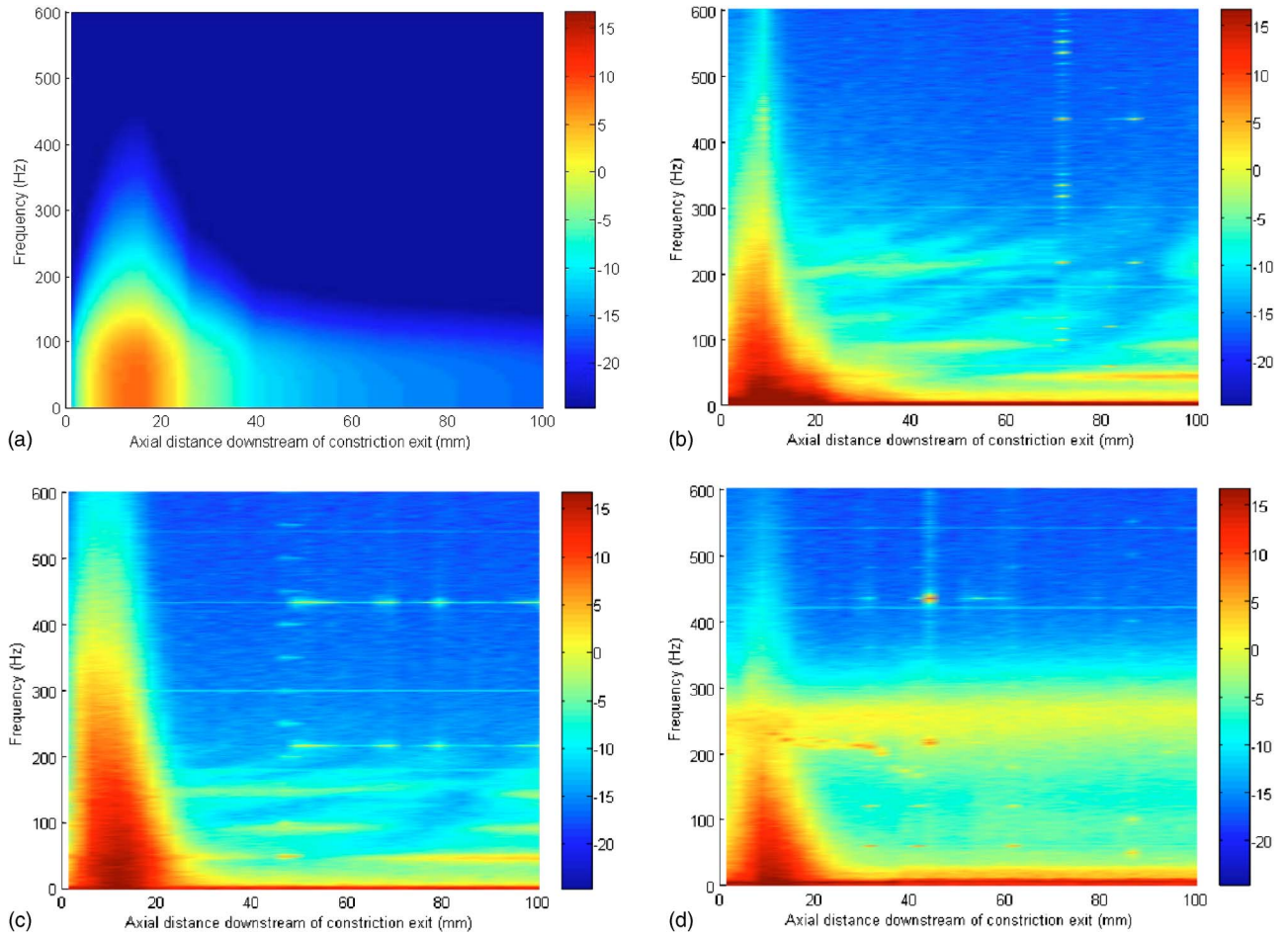

FIG. 2. (Color online) Acoustic pressure (dB *re*: 1 Pa) near wall inner surface as function of axial position and frequency for $Re_D=1000$. All cases are for a tube with a constriction ending at 0 mm. (a) Theory. (b) Experiment in compliant tube in air. (c) Experiment in compliant tube in water. (d) Experiment in rigid tube. Online version uses color scale for dB.

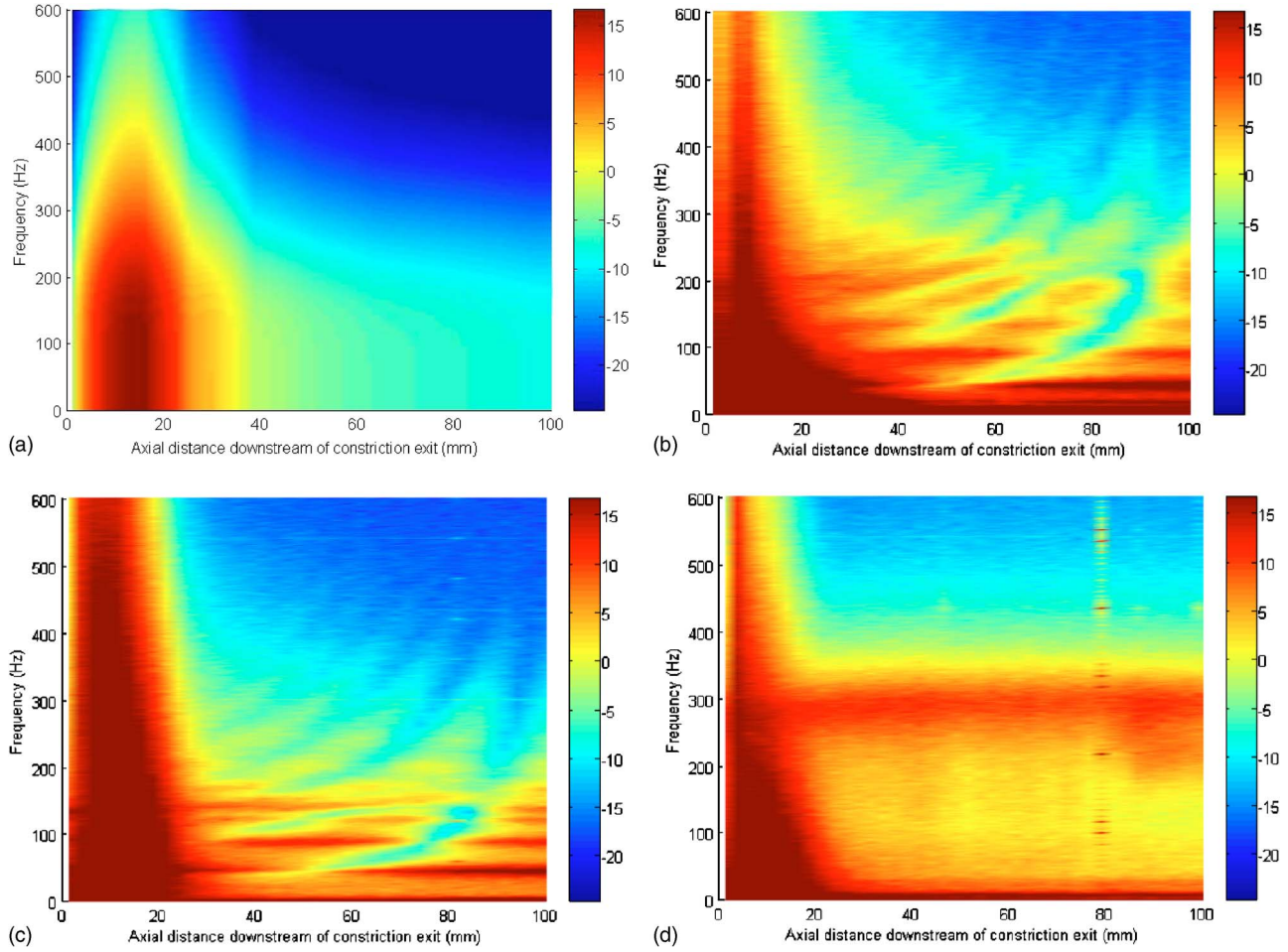

FIG. 3. (Color online) Acoustic pressure (dB *re*: 1 Pa) near wall inner surface as function of axial position and frequency for $\mathrm{Re}_D=2000$. All cases are for a tube with a constriction ending at 0 mm. (a) Theory. (b) Experiment in compliant tube in air. (c) Experiment in compliant tube in water. (d) Experiment in rigid tube. Online version uses color scale for dB.

was estimated to have an elastic modulus at the upper limit of the vascular physiological range, though no specific tube material property values were provided. The blunt and axisymmetric constriction was 12.7 mm long, and five different d/D ratios resulting in 75% to 95% reductions in area were considered. A wall pressure tap of diameter 1.75 mm was located downstream of the stenosis. Flow velocities, U, ranging from 60–500 mm/s and associated Reynolds numbers, based on D and U (Re_D) of 500–4000 were considered. The pressure sensor used at the tap was capable of measuring the dynamic response at least up to 2000 Hz.

For a range of $\mathrm{Re}_D=1500$ to 4000 they found a fairly consistent relationship between the dynamic root-mean-square wall pressure p_{rms} and the distance x downstream from the stenosis such that

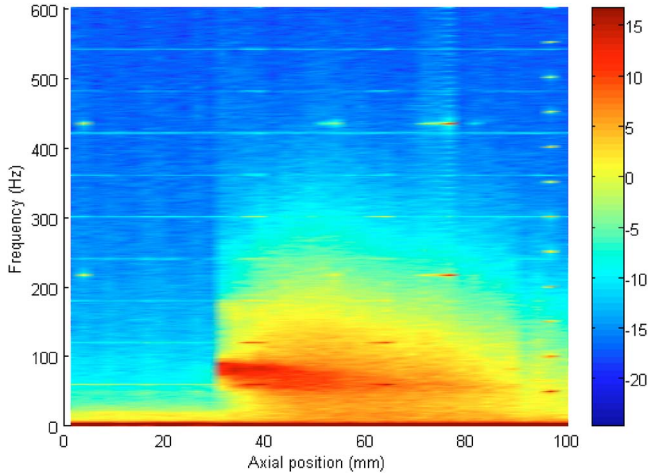

FIG. 4. (Color online) Acoustic pressure (dB *re*: 1 Pa) near wall inner surface as function of axial position and frequency for $\mathrm{Re}_D=2000$ in an *unconstricted* compliant tube (experiment). Online version uses color scale for dB.

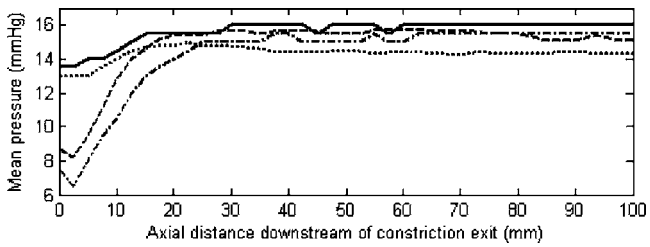

FIG. 5. Constricted tube mean fluid pressure (mm Hg gauge) as a function of axial position. Key: ——— $\mathrm{Re}_D=1000$, compliant tube; --- $\mathrm{Re}_D=1000$, rigid tube; – – – $\mathrm{Re}_D=2000$, compliant tube; –·– $\mathrm{Re}_D=2000$, rigid tube.

$$p_{\mathrm{rms}} = \rho u_j^2 \frac{d}{D} F_{n1}[x/D], \tag{1}$$

where F_{n1} denotes a nonlinear relationship, ρ is the fluid density, u_j is the spatial mean systolic jet velocity in the constriction, and x is the distance downstream from the end of the constriction.

For this same range of Reynolds numbers and constrictions, Tobin and Chang[9] also identified a consistent relationship between the power spectral density $E(f)$ and frequency f at the position x/D, where p_{rms} is maximum such that

$$E(f) \equiv \frac{p(f)^2}{\Delta f} = \rho^2 D u_j^3 \left(\frac{d}{D}\right)^2 F_{n2}[fD/u_j], \tag{2}$$

where F_{n2} denotes a nonlinear monotonic relationship and $p(f)^2/\Delta f$ denotes the power spectral density of the wall pressure variation as a function of frequency f and dependent on the filter bandwidth that was used, such that the units are pascals^2/Hz. As the nondimensional frequency increases (beyond the corner frequency) the log–log spectra approach a negative slope of 5.3. Specifically, a curve fit to the data in Ref. 9 yields

$$F_{n2}[fD/u_j] = \frac{0.002\,08}{1 + 20(fD/u_j)^{5.3}}. \tag{3}$$

Also, note that

$$p_{\mathrm{rms}}^2 = \langle p(t)^2 \rangle = \left(\frac{1}{T}\int_0^T p(t)^2 dt\right) = \int_0^\infty E(f) df, \tag{4}$$

where T is a suitable averaging time such that the value has asymptotically converged. The above formula can be used to approximate, let's say, the root-mean-square pressure value between frequencies $f - \frac{1}{2}$ Hz and $f + \frac{1}{2}$ Hz such that

$$p_{\mathrm{rms}}(f) \approx \rho D^{1/2} u_j^{3/2} \left(\frac{d}{D}\right) (F_{n2}[fD/u_j])^{1/2}. \tag{5}$$

Next, by taking the spectral content in this 1-Hz band to be concentrated at f and in phase, one could express this component of the spectrum in the following form:

$$p(e^{j2\pi ft}, \phi_f) = \sqrt{2}\rho U^{3/2} \frac{D^{5/2}}{d^2} (F_{n2}[fd^2/UD])^{1/2} e^{j(2\pi ft + \phi_f)}. \tag{6}$$

In this expression the term ϕ_f denotes an unknown phase angle. Under this condition, and taking x/D at the point of the maximum value for p_{rms}, then, based on Fig. 12 of Ref. 9

$$p_{\mathrm{rms}} \approx \left(\sum_{f=1}^{\infty} (p[e^{j2\pi ft}, \phi_f])^2\right)^{1/2} \approx \rho U^2 \frac{D^3}{d^3} F_{n1}[x_{\max}/D]$$
$$\approx \rho U^2 \frac{D^3}{d^3}(0.0355). \tag{7}$$

According to Ref. 9, the spectral distribution of the wall pressure variation at different downstream positions maintains the same general form as at the point of maximum p_{rms}, but does vary to some degree. Specifically, as one moves downstream from near the position of maximum pressure, both the amplitude and corner frequency of the spectrum decrease. However, quantitative measurements are not provided. In the present treatment, it will be assumed that the relative spectral distribution will stay the same, but be attenuated in overall amplitude to correctly follow the p_{rms} level as it decreases when one moves away from its maximum location.

Specifying a value for ϕ_f is another matter. This issue is taken up in some detail by Keith and Abraham[23] for the more general case of turbulent pressure flow over a wall. The baseline assumption is that the turbulent wall pressure convection velocity u_c matches that of the stream velocity. Owsley and Hull[18] have assumed that the turbulent wall pressure convection moves axially at the jet velocity u_j of the stenotic constriction. Then, one would have that the phase difference, $\Delta\phi_f$, as a function of frequency f between two points separated by a distance Δx would equal $2\pi f \Delta x/u_j$. However, studies have shown that this simplifying assumption results in an overprediction of cross-spectral properties between two different axial locations of wall pressure measurement. Its effect on predictions of sound radiation to points exterior to the flow tube is unclear. A more accurate model would account for the fact that, near the wall, flow is slower than along the central axis of the flow tube. Larger, coherent structures of lower frequency are located more toward the axial center with smaller structures near the wall. The small structures, however, dissipate more rapidly with distance from the stenosis, and the larger structure's effect on wall pressure variations may become relatively more prominent further downstream. It follows that u_c may be a complex, frequency-dependent quantity. In the present study, the approximation used by Owsley and Hull[18] is followed.

These assumptions lead to

$$p[e^{j2\pi ft}, x, \phi_f] = P_0 e^{j(2\pi f - \phi_f)} = 1.82 F_{n1}[x/D]\rho U^{3/2} \times \frac{D^{5/2}}{d^2}\left(\frac{1}{1 + 20(fd^2/UD)^{5.3}}\right)^{1/2} e^{j(2\pi ft - \phi_f)}, \tag{8a}$$

where

$$\phi_f[f, x] = \frac{2\pi f x d^2}{UD^2}. \tag{8b}$$

Here, $F_{n1}[x/D]$ is the value interpolated from Fig. 12 of Tobin and Chang.[9] Linear interpolation via a tabular approximation was used in simulations reported here and is provided in Table II. Note that the studies in Ref. 9 were conducted with different flow constrictions and upstream pressures to achieve different Reynold's numbers and percent area stenoses. Apparently, no attempt was made to ensure that the mean pressure downstream of the constriction was consistent.

B. Theoretical predictions and experimental measurements

Based on the above theoretical analysis, and given the geometry of the experimental system provided in Fig. 1 and

Table I, predictions of the acoustic pressure on the wall inner surface as a function of axial distance downstream of the constriction exit and as a function of frequency were computed [Figs. 2(a) and 3(a)] for flows with Re_D of ~1000 and ~2000. (This calculation is made neglecting a ~2.8% increase in D in the compliant tube due to the internal mean pressure of ~15 mm Hg.) This corresponds to Reynold's numbers in the rigid constricted zone of Re_d equals 2783 and 5565, respectively. It is apparent that the greatest acoustic pressure amplitude occurs roughly 15 mm downstream of the constriction exit for both cases. Spectral content up through several hundred hertz is significant, but then attenuates at higher frequencies.

As described in Sec. II B, internal mean and dynamic pressure measurements were made using a miniature catheter hydrophone. It is recognized that the presence of the hydrophone likely will alter the flow field. Additionally, the hydrophone is not acquiring a pressure measurement directly at the channel inner wall, but rather at a location within the flow channel near the wall. Measurements were obtained for flow rates of Re_D= ~1000 and ~2000, within the compliant latex tube, as well as within a more rigid, hard plastic tube of the same inner dimensions, in order to assess the effect of tube wall compliance on the flow field. Measurements were also obtained in compliant and "rigid" tubes with the axisymmetric flow constriction removed.

Selected results are presented in Figs. 2–5. In comparing theoretical predictions to experiment, it appears that the theory has captured some of the general trends, both in terms of amplitude and spatial-spectral distribution, though the match is not perfect. In the experiment, the maximum pressure appears to be closer to 10–13 mm downstream of the constriction, as opposed to 15 mm. This discrepancy may be due in part to the hydrophone position. As the turbulent field spreads radially after exiting the constriction, it will reach the hydrophone before it reaches the tube wall. Additionally, the presence of the hydrophone may cause turbulence to occur earlier at a position further upstream.

There are other downstream spatial-spectral features evident in the experimental measurement that are not evident in the theoretical predictions, particularly observable in the Re_D=2000 case. In comparing experimental measurements for the constricted compliant tube versus a constricted rigid tube, the downstream spectral content is very different, which suggests that it is coupled with the tube wall dynamics. Note that the band of increased vibration that occurred along the entire length of the rigid test section at around 250–300 Hz was also present, though to a far less extent, for a rigid tube *without* a flow constriction (measurements not shown). An experimental modal analysis of the test setup indicated that a beamlike bending resonance of the rigid tube was present with a spectral peak in the 250–300 Hz range; it is suspected that this resonance may have been excited by flow dynamics and in turn increased the spectral content of the dynamic pressure measured in the fluid.

For the compliant tube cases, multiple bands of increased vibration along the length of the axis appear; these generally disappear, or at least recede to below the noise floor when the constriction is removed. These bands, which are not predicted by theory, are not due to the presence of the hydrophone in the flow channel, as they also appear to affect the vibration of the compliant tube (shown later) even when the hydrophone was not inserted. (In all constricted compliant studies, vibration of the compliant tube was identical with respect to whether or not the hydrophone was present.) Additionally, axisymmetric resonant modes of tube vibration are evident in the pressure readings, particularly in Figs. 3(b) and 3(c). Note that in one unconstricted study in the compliant tube at Re_D=2000, when the hydrophone was placed at roughly 30 to 100 mm from the compliant tube entrance, turbulence was generated that appeared to be caused by the hydrophone's presence (Fig. 4). For the same unconstricted test in a rigid tube, no turbulence occurred. Likewise, at Re_D=1000, in rigid and compliant tubes without constrictions, no turbulence occurred.

Overall, spectral bands downstream of the constriction do appear to be altered by the flow rate (Re), whether the tube is rigid or compliant, and, in the case of the compliant tube, also depend on the mean fluid pressure and whether external fluid loading is present. Hence, they are associated with coupled fluid and structural dynamics, which are not captured using the simple theory proposed here and likely would not be accurately predicted using a more complex theory or numerical (CFD) simulation that did not account for compliant walls. While the mean pressure did drop immediately downstream of the constriction (Fig. 5), it remained above atmospheric pressure in this experiment, and large deformation buckling or tube collapse was not observed.

IV. FLUID–VESSEL COUPLING

A. Theory

1. Tube of infinite length

Consider a cylindrical tube of radius "a" and thickness "h" that is infinite in length. It will be assumed that the tube material is isotropic, and the tube itself can be considered to be thin (e.g., $h/a<0.1$). Extensions of the analysis to the case of orthotropy[24] and "thick shell" theory are relatively straightforward but introduce additional complexity that is not relevant to the present analysis. The vibrational motion of a thin, isotropic cylindrical elastic shell can be described by the Donnell–Mushtari (DM) equations.[25] In addition to the assumption that h/a is small, this theory also assumes that resulting shell dynamic displacements are small, transverse normal stress acting on planes parallel to the shell middle surface are negligible, and fibers of the shell normal to the middle surface remain so after deformation and are themselves not subject to elongation. Presence of a compressible fluid within and/or exterior to the shell and the resulting fluid–structure interaction has been considered.[26–29] Alternative derivations for thicker shells have been applied to this problem with interior fluid, including use of the Kennard shell equations, which add a few additional terms to account for curvature but do not increase the degrees of freedom.[28] Use of first-order shear deformation theory to augment the DM theory, which adds two rotational degrees of freedom to account for shear deformation through the

shell thickness, has also been considered in conjunction with compressible fluid interior and exterior to the shell.[29]

Consider harmonic line forces applied around the circumference of the tube at axial position x_0 and specified by

$$p_t(x_0,\theta,t) = F_t \cos(n\theta)\delta(x-x_0)e^{j\omega t}, \tag{9}$$

where F_t is force per unit length, δ denotes the Dirac delta function, θ is the azimuthal angle in the tube with $\theta=0$ denoting vertically up, $\omega=2\pi f$, and $n=0,1,2,\ldots$. The excitation of the tube wall due to interior turbulent flow is approximated by resolving it into a finite number of such line forces. Given the case of harmonic excitation, it is convenient to express the shell displacements and applied forces in terms of inverse Fourier transforms in the axial wave number k_{ns}, here taking the case that $x_0=0$.[27]

$$u = \frac{1}{\sqrt{2\pi}}\sum_{n=0}^{\infty}\sum_{s=0}^{\infty}\int_{-\infty}^{\infty}\bar{U}_{ns}\cos(n\theta)e^{j(-k_{ns}x+\omega t+\pi/2)}\partial k_{ns}, \tag{10}$$

$$v = \frac{1}{\sqrt{2\pi}}\sum_{n=0}^{\infty}\sum_{s=0}^{\infty}\int_{-\infty}^{\infty}\bar{V}_{ns}\sin(n\theta)e^{-j(k_{ns}x-\omega t)}\partial k_{ns}, \tag{11}$$

$$w = \frac{1}{\sqrt{2\pi}}\sum_{n=0}^{\infty}\sum_{s=0}^{\infty}\int_{-\infty}^{\infty}\bar{W}_{ns}\cos(n\theta)e^{-j(k_{ns}x-\omega t)}\partial k_{ns}, \tag{12}$$

$$\bar{p}_t = (1/\sqrt{2\pi})F_t\cos(n\theta)e^{j\omega t}. \tag{13}$$

Here, u, v, and w denote vibratory displacements in the axial, azimuthal, and radial directions, respectively. One obtains the following by inserting these expressions into the DM equations and utilizing orthogonality of the n and s components in the summations in Eqs. (10)–(12):

$$\begin{bmatrix} L_{11} & L_{12} & L_{13} \\ L_{21} & L_{22} & L_{23} \\ L_{31} & L_{32} & L_{33} \end{bmatrix}\begin{bmatrix} \bar{U}_{ns} \\ \bar{V}_{ns} \\ \bar{W}_{ns} \end{bmatrix} = \begin{bmatrix} 0 \\ 0 \\ \Omega^2 F_t/\sqrt{2\pi}\rho_s h\omega^2 \end{bmatrix}, \tag{14}$$

with

$$L_{11} = -\Omega^2 + (k_{ns}a)^2 + n^2\left(\frac{1-\nu}{2}\right), \tag{15a}$$

$$L_{12} = L_{21} = n(k_{ns}a)\left(\frac{1+\nu}{2}\right), \tag{15b}$$

$$L_{13} = L_{31} = \nu(k_{ns}a), \tag{15c}$$

$$L_{22} = -\Omega^2 + \frac{1-\nu}{2}(k_{ns}a)^2 + n^2, \tag{15d}$$

$$L_{23} = L_{32} = n, \tag{15e}$$

and

$$L_{33} = 1 + \beta^2[(k_{ns}a)^2 + n^2]^2 - \Omega^2 - FL_i - FL_e, \tag{15f}$$

where FL_i and FL_e, respectively, account for internal and external fluid loading in the coupled problem. It is assumed that these are compressible fluids that satisfy the acoustic wave equation in cylindrical coordinates. To ensure the fluid remains in contact with the tube wall, the fluid radial motion and the tube radial motion must be equal at the interface of the tube and fluid. If the shell is submerged in a compressible fluid of infinite extent, this coupling condition results in the following expressions:

$$FL_i = \Omega^2\frac{\rho_i}{\rho_s h k_{ri}}\left[\frac{J_n[k_{ri}a]}{J_n'[k_{ri}a]}\right], \tag{16}$$

$$FL_e = \Omega^2\frac{\rho_e}{\rho_s h k_{re}}\left[\frac{H_n^{(2)}[k_{re}a]}{H_n'^{(2)}[k_{re}a]}\right], \tag{17}$$

where

$$\Omega^2\left(\frac{c_L}{c_i}\right)^2 = (k_{ns}a)^2 + (k_{ri}a)^2, \tag{18a}$$

$$\Omega^2\left(\frac{c_L}{c_e}\right)^2 = (k_{ns}a)^2 + (k_{re}a)^2, \tag{18b}$$

$$\Omega = \omega a/c_L, \tag{18c}$$

and

$$c_L = \sqrt{E(1+j\omega\xi)/\rho_s(1-\nu^2)}. \tag{18d}$$

Here, J_n and $H_n^{(2)}$, respectively, refer to an nth-order Bessel function of the first kind and an nth-order second Hankel function, which denotes outgoing wave propagation consistent with the convention $e^{j\omega t}$ denoting harmonic motion. Also, the primes on J_n and $H_n^{(2)}$ denote differentiation with respect to the arguments $k_{ri}a$ and $k_{re}a$, respectively. If the external fluid does have finite boundaries, then the expression in Eq. (17) would need to be modified. Additionally, ρ_s, ρ_i, and ρ_e refer to the density of the shell (tube) material, internal fluid, and external fluid, respectively. And, c_L refers to the complex extensional phase speed of the tube material, dependent on its Young's modulus, E, linear viscous loss factor, ξ, density, ρ_s, and Poisson's ratio ν.

Then, the spectral radial displacement amplitude [as a function of $(k_{ns}a)$] is

$$\bar{W}_{ns} = \left(\frac{\Omega^2 F_t}{\sqrt{2\pi}\rho_s h\omega^2}\right)I_{33}, \tag{19a}$$

where

$$I_{33} = (L_{11}L_{22} - L_{12}L_{21})/|\mathbf{L}|. \tag{19b}$$

Application of the inverse transform gives the radial displacement as

$$w(x/a,n,s) = \frac{\Omega^2 F_t}{2\pi\rho_s h a\omega^2}\int_{-\infty}^{\infty} I_{33}e^{-j(k_{ns}a)(x/a)}d(k_{ns}a) = Y_{ns}(x/a)F_0/j\omega, \tag{20}$$

where $Y_{ns}(x/a)$ is the transfer mobility for a particular branch s and circumferential mode of vibration n such that

$$\frac{\dot{w}(x/a,n,s)}{F_t} = Y_{ns}(x/a)$$

$$= \frac{j\Omega^2}{2\pi\rho_s ha\omega}\int_{-\infty}^{\infty} I_{33}e^{-j(k_{ns}a)(x/a)}d(k_{ns}a). \quad (21)$$

By utilizing the theorem of residues, the transfer mobility (i.e., response at x due to excitation at $x_0=0$) can be written as the sum of the residues evaluated at the poles: i.e.,

$$Y_{ns}(x/a) = \frac{\Omega^2}{\rho_s ha\omega}\sum_{s=1}^{\infty} \text{Re } s_s, \quad (22a)$$

$$\text{where Re } s_s = \frac{(L_{11}L_{22} - L_{12}L_{21})e^{-j(k_{ns}a)(x/a)}}{(\det|L|)'}, \quad (22b)$$

where the prime denotes the derivative with respect to $(k_{ns}a)$.

To couple this analysis with the analysis of the turbulent field in the previous section, the line force F_t is obtained by taking the axisymmetric ($n=0$) pressure calculation from the turbulent analysis and approximating it as a circumferential line force in terms of short segments along the cylinder. So, $F_t=P_0^{\star}\Delta L$, where ΔL is made small enough that the results asymptotically converge. Note that, if pressure data were available from, say a numerical simulation that involved a nonaxisymmetric constriction and a resulting nonaxisymmetric pressure distribution, higher azimuthal order ($n>0$) components could be used to predict the resulting nonaxisymmetric tube vibration.

2. Tube of finite length

The compliant section of tube of length L in the experimental setup (Fig. 1) is approximated as pinned at its ends such that simply supported boundary conditions exist. Adapting the above analysis for the harmonic line force and finite length shell yields

$$u = \sum_{n=0}^{\infty}\sum_{m=1}^{\infty} U_{nm}\cos(m\pi x/L)\cos(n\theta)e^{j\omega t}, \quad (23)$$

$$v = \sum_{n=0}^{\infty}\sum_{m=1}^{\infty} V_{nm}\sin(m\pi x/L)\sin(n\theta)e^{j\omega t} \quad (24)$$

$$w = \sum_{n=0}^{\infty}\sum_{m=1}^{\infty} W_{nm}\sin(m\pi x/L)\cos(n\theta)e^{j\omega t}. \quad (25)$$

Again, by insertion of these expressions into the DM equations and utilizing the orthogonality of the mode shapes, delineated by m and n, this leads to

$$\begin{bmatrix} L_{11} & L_{12} & L_{13} \\ L_{21} & L_{22} & L_{23} \\ L_{31} & L_{32} & L_{33} \end{bmatrix}\begin{bmatrix} U_{nm} \\ V_{nm} \\ W_{nm} \end{bmatrix} = \begin{bmatrix} 0 \\ 0 \\ 2\Omega^2 F_t \sin(k_m x_0)/L\rho_s h\omega^2 \end{bmatrix}, \quad (26)$$

with

$$L_{11} = -\Omega^2 + (k_m a)^2 + n^2\left(\frac{1-\nu}{2}\right), \quad (27a)$$

$$L_{12} = L_{21} = -n(k_m a)\left(\frac{1+\nu}{2}\right), \quad (27b)$$

$$L_{13} = L_{31} = -\nu(k_m a), \quad (27c)$$

$$L_{22} = -\Omega^2 + \frac{1-\nu}{2}(k_m a)^2 + n^2, \quad (27d)$$

$$L_{23} = L_{32} = n, \quad (27e)$$

and

$$L_{33} = 1 + \beta^2[(k_m a)^2 + n^2]^2 - \Omega^2 - FL_i - FL_e. \quad (27f)$$

The internal and external fluid loading terms, FL_i and FL_e, would be the same as in the infinite case if rigid diaphragms existed at $x=0$ and $x=L$ extending from $r=0$ to ∞ for $\theta=0$ to 2π; this is not the case in the experimental setup. Consider the internal loading term first, FL_i. At $x=0$ the axisymmetric constriction exists at the connection of the rigid tube to the compliant tube, resulting in an impedance mismatch. At $x=L$, while an axisymmetric constriction does not exist, there is a change from a compliant to a rigid wall, which results in an impedance mismatch. These end impedances are not infinite, which would be the case if rigid diaphragms existed. This difference is expected to have a more significant effect at lower axial modal orders, with reducing significance as axial modal order increases, since boundary conditions become less important as modal order increases. Nonetheless, in the present theoretical study rigid diaphragms in the internal fluid at $x=0$ and L are assumed, and Eq. (16) is used with the following in place of Eq. (18a):

$$\Omega^2\left(\frac{c_L}{c_i}\right)^2 = (k_{nm}a)^2 + (k_{ri}a)^2. \quad (28)$$

With regard to the external fluid loading term, FL_e, for the experimental case the external fluid extends much less than the wavelength of sound in it; thus, its effect on tube vibrations is approximated simply as a mass load. This leads to

$$FL_E = \Omega^2\frac{\rho_e}{\rho_s}\frac{h_{eq}(h_{eq}+2a)}{2ha}, \quad h_{eq} = a + h_g + h/2, \quad (29)$$

where h_g denotes the depth from the top of the tube to the free surface of the external fluid. This expression is equivalent to adding to the tube a mass per unit length representing an external fluid layer of thickness h_{eq} completely surrounding the tube, where h_{eq} is the average distance of a point on the tube wall to the nearest free surface.

Radial velocity of the tube at axial location x and angular position θ due to the circumferential line force per unit length F_t at $x=x_0$ can then be expressed in terms of a modal superposition

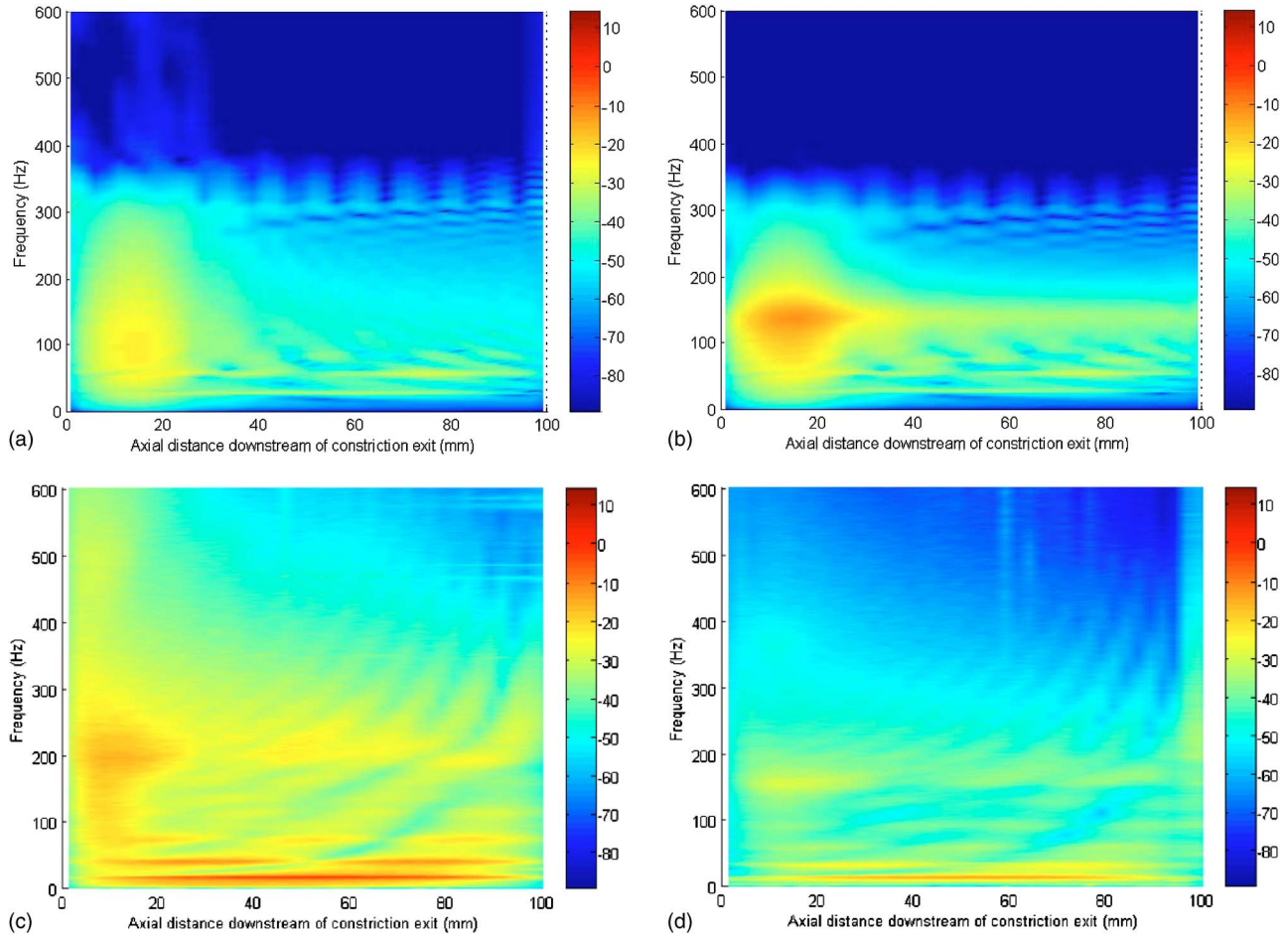

FIG. 6. (Color online) Constricted compliant tube radial wall velocity (dB *re*: 1 mm/s) as a function of axial position and frequency for $\mathrm{Re}_D=1000$. (a) Theory, in air. (b) Theory, submerged in water. (c) Experiment, in air. (d) Experiment, submerged in water. Online version uses color scale for dB.

$$\dot{w}[x,\theta,t]=\sum_{n=0}^{\infty}\sum_{m=1}^{\infty} I_{33} j\omega \frac{2\Omega^2 F_t \sin[k_m x_0]}{L\rho_s h\omega^2} \times \sin(m\pi x/L)\cos(n\theta)e^{j\omega t}, \tag{30}$$

where I_{33} is given by Eq. (19b) with values of $\mathbf{L}$ defined in Eqs. (26) and (27).

B. Theoretical predictions and experimental measurements

The predicted axisymmetric pressure distribution from Sec. III was used as an input to the finite-length tube model to predict the resulting vessel wall axisymmetric radial velocity $\dot{w}$ as a function of axial position and frequency. Circumferential line forces per unit length $F_t(x,f)$ were used every 1.2 mm axially to approximate $p_t(x,f)$, whose magnitude was depicted in Figs. 2(a) and 3(a). Theoretical predictions are shown in Figs. 6(a), 6(b), 7(a), and 7(b) for the flow cases of $\mathrm{Re}_D=1000$ and 2000 for the case of only internal fluid (fluid-filled tube suspended in air), and for the case of internal and external fluid. Also shown in these same figures are the corresponding experimental measurements of the tube wall vibration, using laser Doppler vibrometry; see Figs. 6(c), 6(d), 7(c), and 7(d). In comparing experimental cases without and with external fluid loading, it appears that the external fluid loading is primarily acting as a mass load, decreasing the frequency of, but not altering, the spatial-spectral character of the system. Likewise, in comparing similar cases with $\mathrm{Re}_D=1000$ vs $\mathrm{Re}_D=2000$, the change in flow rate appears to alter the intensity of vibration significantly, but it alters the spatial-spectral distribution of the vibration less significantly. This emphasizes the importance of the surrounding structural dynamic properties, which are consistent and unchanged when flow rate changes.

In comparing the theoretical cases to the experimental cases, again it appears that some but not all phenomena are captured. Even if one takes the experimental pressure measurements shown in Figs. 2(b), 2(c), 3(b), and 3(c) and uses these as an input to the theoretical tube model of Sec. IV, a closer, but still not exact match to experiment can be achieved. (Results of this "hybrid" calculation are not shown.) In the theoretical simulation, all geometric and material parameters (Table I) were measured or identified independently of this experiment, except the linear viscous damping term used for latex, ξ; this value was adjusted based on a rough comparison of theory and experiment, but was kept the same in all simulations. Use of a material damping term with a nonlinear dependence on frequency would have improved the match between theory and experiment. Also, during the course of the experimental study, three different latex tubes were used and some variability of elastic modulus, up to 10%, was observed between different tubes and as

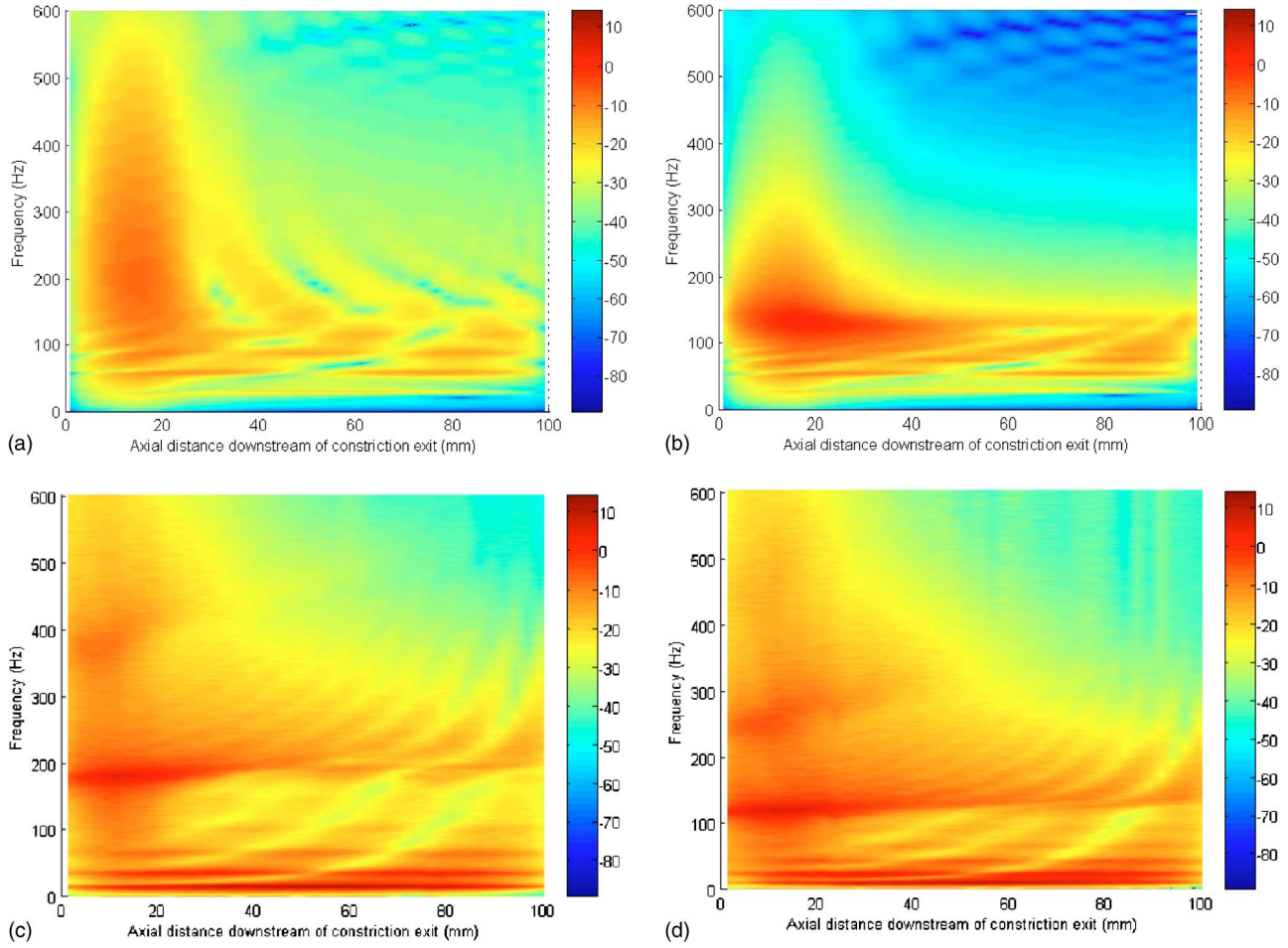

FIG. 7. (Color online) Constricted compliant tube radial wall velocity (dB *re*: 1 mm/s) as a function of axial position and frequency for $\mathrm{Re}_D=2000$. (a) Theory, in air. (b) Theory, submerged in water. (c) Experiment, in air. (d) Experiment, submerged in water. Online version uses color scale for dB.

a function of time in the same tube due to usage and aging; Young's modulus would decrease slightly after repeated use.

Some experimentally observed dynamics are simply not captured in the theoretical treatment. It is suspected that the mean pressure drop immediately after the constriction (see Fig. 5) does alter the system somewhat in this region, relative to the theoretical model, which assumed a uniform mean pressure throughout the length of the compliant tube in determining tube dimensions. As predicted above, due to the implicit assumption of rigid diaphragms in the fluid at either end of the flexible tube, the lowest tube structural resonant modes for the experiment tend to shift down in frequency, relative to theory, though for modes above the first three, agreement between theory and experiment is good.

For the experimental cases shown in Figs. 6 and 7, the mean (head) pressure in the compliant tube was adjusted to ~15 mm Hg gauge by adjusting the height of the upstream reservoir. It was found that increasing the mean pressure in the fluid channel substantially increased some, but not all, of the spectral features of the tube vibration. Figure 8 shows a case for $\mathrm{Re}_D=1000$ with the compliant constricted tube in air (no external water or gel loading), but with an internal mean pressure of ~60 mm Hg gauge. The conditions of this case are identical to that shown in Fig. 6(c) except for the increase in mean pressure of ~45 mm Hg. Such a change in pressure increases the compliant tube diameter by ~8.4% and decreases its thickness by ~7.7%; this should lower axisymmetric tube structural resonances by about 7% assuming linear elasticity. Static tests of tube diameter as a function of

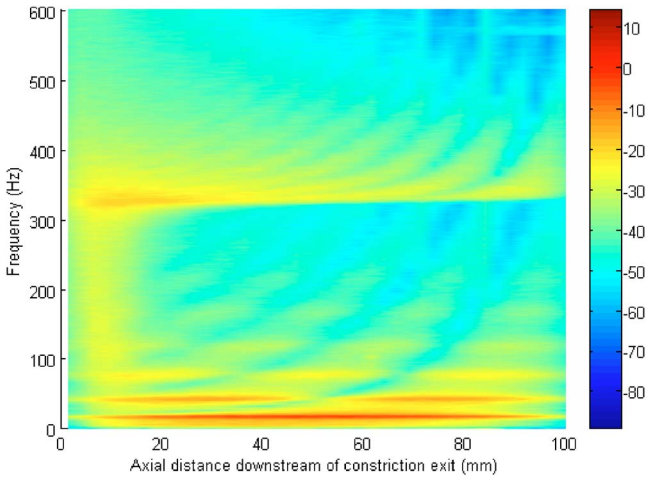

FIG. 8. (Color online) Measured constricted compliant tube radial wall velocity (dB *re*: 1 mm/s) as a function of axial position and frequency for $\mathrm{Re}_D=1000$, in air. Effect of head pressure. High tank (Fig. 1) at same height as in $\mathrm{Re}_D=2000$ case resulting in downstream mean pressure of ~60 mm Hg gauge. Online version uses color scale for dB.

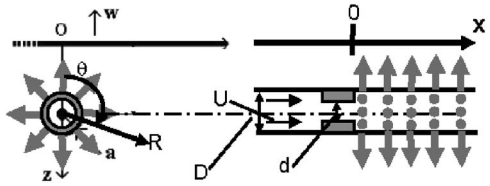

FIG. 9. Approximating the radiation of vibro-acoustic energy from the flexible tube vibration with finite dipoles.

internal static pressure confirmed that the tube elasticity was slightly nonlinear, with a ~10% increase in elastic modulus when internal pressure increased from 15 to 60 mm Hg. This increase actually would counter the effect of the geometric changes and result in less of a predicted decrease in resonant frequency. Significant changes are not evident in the frequencies of the first few standing wave patterns for the tube, below 100 Hz, supporting this analysis.

However, at higher frequencies, there is a significant change in the spectral content between the two cases [Figs. 6(c) and 8]. This same trend was observed in a number of experiments at various Re_D and mean pressures. While increasing the mean pressure did not significantly alter the lower frequency standing wave response of the tube, it did increase the frequency and sometimes sharpen the spectral content of the higher frequency vibration that was strongest just downstream of the constriction (from ~200 to ~325 Hz for $\mathrm{Re}_D=1000$ at 15 and 60 mm Hg mean pressure, respectively). Theoretical simulations, which used different values for diameter and thickness of the tube dependent on the mean pressure, showed no significant changes in their prediction of the internal dynamic pressure and tube vibration when the internal mean pressure was varied from 15 to 60 mm Hg. It is hypothesized that the observed phenomenon is due to nonlinear behavior just downstream of the constriction that is caused in part by the larger dynamic forces at this point and the substantially reduced mean pressure immediately distal to the constriction, shown in Fig. 5. Such behavior in a collapsible tube has been previously demonstrated.[22]

V. RADIATION INTO THE SURROUNDING VISCOELASTIC MEDIUM

A. Theory

Now, consider the axisymmetrically vibrating tube to be embedded in a viscoelastic phantom material with properties comparable to soft biological tissue. The term for external fluid loading, given above in Eq. (29), may be suitable when, in fact, the external medium is a fluid. However, when the tube is embedded parallel to and near the surface of a viscoelastic medium, a different approach may be considered. The elastic and viscous forces of the viscoelastic material may be non-negligible. Consequently, a composite tube wall is defined as being composed of the latex material and a thickness of the gel material taken to be the depth that the latex is below the free surface, h_g. The composite tube thickness h_c is thus the combined thickness of the latex material h and its depth below the surface, h_g. The composite Young's

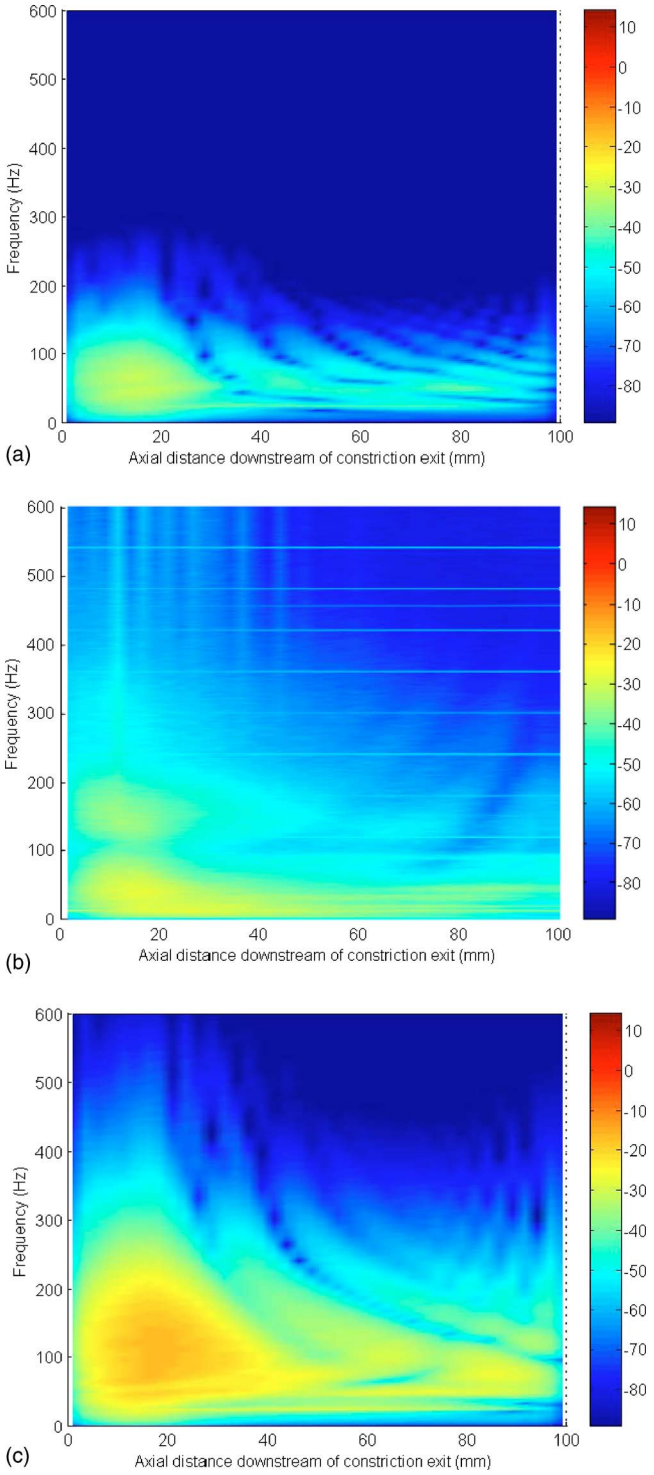

FIG. 10. (Color online) Constricted compliant tube radial wall velocity (dB *re*: 1 mm/s) while embedded in soft tissue gel phantom as a function of axial position and frequency. (a) Theory, $\mathrm{Re}_D=1000$. (b) Experiment, $\mathrm{Re}_D=1000$. (c) Theory, $\mathrm{Re}_D=2000$. Experimental measurement at $\mathrm{Re}_D=2000$ not possible. Online version uses color scale for dB.

modulus E_c is taken to be that of the thickness-weighted sum of the individual elastic moduli of the Latex and gel material

$$E_c = \frac{h}{h_c}E_L + \frac{h_g}{h_c}E_g, \tag{31}$$

with $E_g \approx 3\mu$, where μ is the complex shear modulus of the gel phantom material (Table I). This is then used in place of

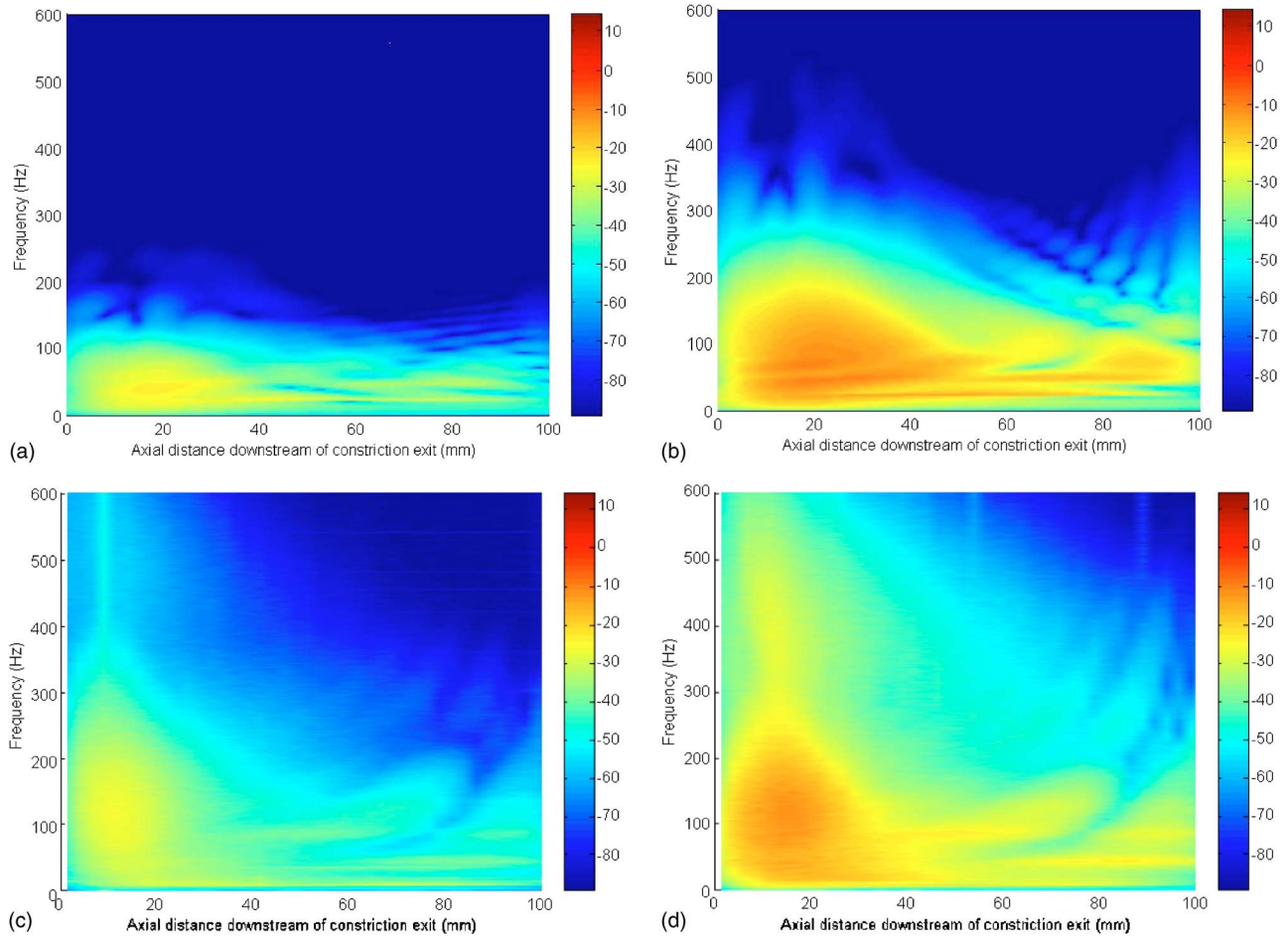

FIG. 11. (Color online) Vertical velocity (dB *re*: 1 mm/s) at phantom surface for constricted compliant tube embedded in soft tissue gel phantom as a function of axial position and frequency directly above tube. (a) Dipole theory, $\mathrm{Re}_D=1000$. (b) Dipole theory, $\mathrm{Re}_D=2000$. (c) Experiment, $\mathrm{Re}_D=1000$. (d) Experiment, $\mathrm{Re}_D=2000$. Online version uses color scale for dB.

E in Eq. (18d) and the term $FL_E=0$. With these assumptions, the radial vibration of the tube wall can be predicted with Eq. (30) and used as the input to a model that will predict the resulting motion at the gel surface. Note that the motion at the phantom surface just above the tube should closely match that of the tube itself for small values of h_g.

Alternatively, to predict vibratory motion at any location on the phantom surface or within the phantom, the axisymmetrically vibrating tube can be approximated via a finite number of elementary acoustic sources, finite monopoles or dipoles, spaced sufficiently close together. Given that the theoretically modeled radial motion of the tube is axisymmetric, a row of monopoles may seem like a logical approach. However, monopoles do not generate shear waves, only compression waves. In the actual experiment, wall motion will be nonaxisymmetric given the random nature of turbulence, which would result in the generation of shear waves in addition to compression waves. Dipoles do radiate both compression and shear waves, and may result in a more realistic simulation in some cases for some frequency regimes. In a previous study, it was shown that, for elementary acoustic sources comparable in dimension to the compliant tube considered here, and just below the surface of a soft-tissue viscoelastic phantom material, the resulting phantom surface motion is composed of contributions from both shear and compression waves, with shear wave contributions being dominant below ~100 Hz and near the source and compression waves becoming dominant above ~150 Hz and as one moves further from the source.[30]

Two simulation approaches, using monopoles or dipoles, are developed here. In either case, scattering of the field of one elementary source caused by another or by itself after reflection from a boundary is neglected. That is, the monopoles and dipoles will be treated as infinitesimal. Additionally, the viscoelastic medium will be considered to be a semi-infinite half-space. The effect of these assumptions on the predicted field for single monopole or dipole sources is discussed in Royston *et al.*[30] Also in Ref. 30, it was shown that, generally as one moves away from being directly over the source, the surface response to an infinitesimal monopole or dipole just below the surface is reasonably approximated by simply doubling the theoretical response at the location of the half-space surface that is calculated based on the assumption of an infinite medium. This approximation, and neglecting multiple reflections from the source, is expected to worsen the match of theory to experiment when measurements are taken directly over the source.

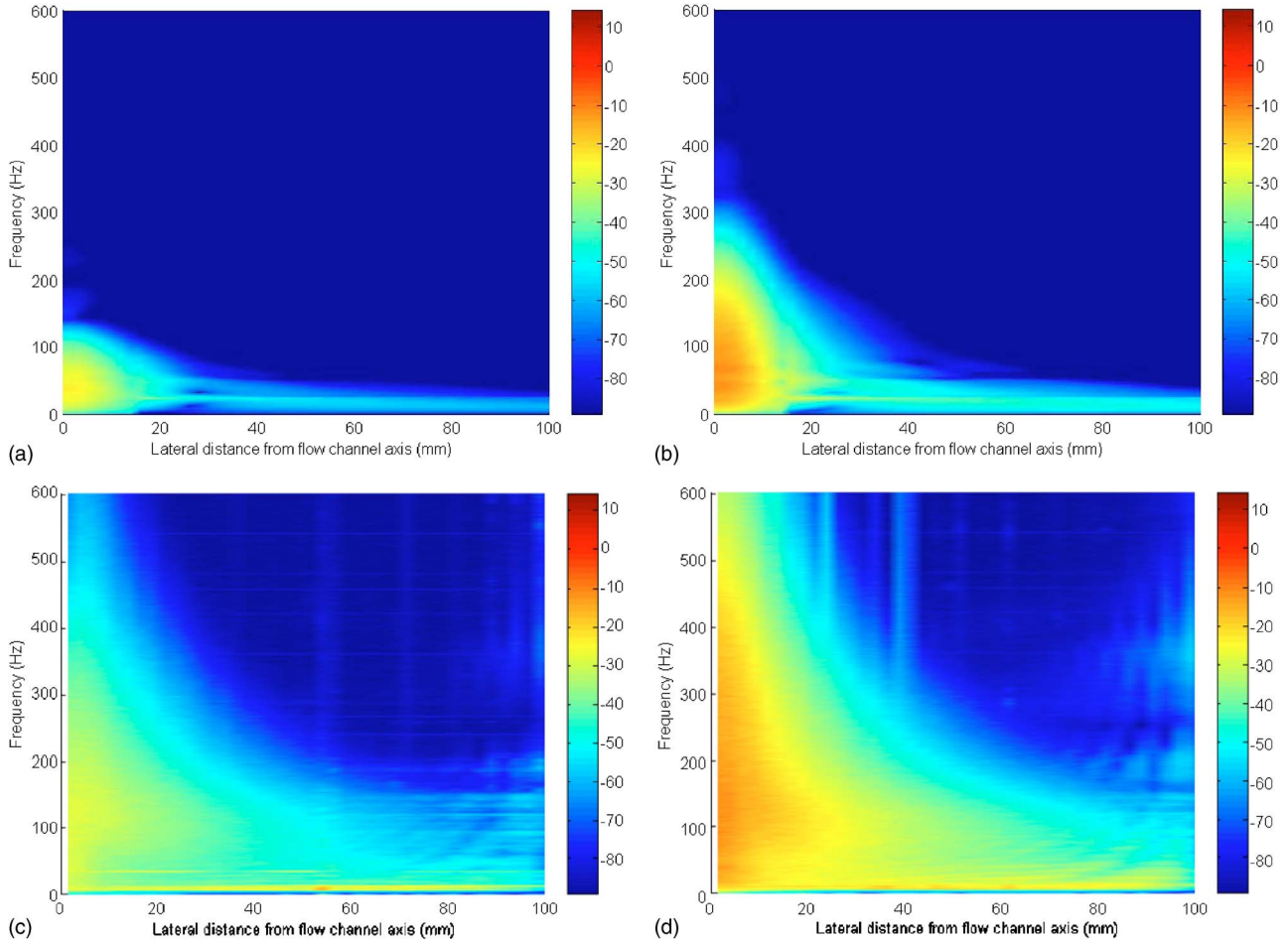

FIG. 12. (Color online) Vertical velocity (dB *re*: 1 mm/s) at phantom surface for constricted compliant tube embedded in soft tissue gel phantom downstream of constriction as a function of lateral position moving away from the tube. (a) Dipole theory at 15 mm downstream, $\mathrm{Re}_D=1000$. (b) Dipole theory at 15 mm downstream, $\mathrm{Re}_D=2000$. (c) Experiment at 10 mm downstream, $\mathrm{Re}_D=1000$. (d) Experiment at 10 mm downstream, $\mathrm{Re}_D=2000$. Online version uses color scale for dB.

1. Monopole approach

For the tube, radial wall velocity is given by Eq. (30). It can be calculated at any axial location x and azimuthal angle θ. Suppose its value is calculated at a finite number of points along the tube with axial resolution ΔL. The calculated radial wall displacement at one of these points w_x is assumed to represent the axisymmetric radial motion of that segment of the tube from $x-\Delta L/2$ to $x+\Delta L/2$. The volume displacement of this segment of the tube will be equated to the volume displacement of a finite monopole of radius a_m undergoing radial displacement of amplitude u_0 and located at the geometric center of the tube segment it represents. This leads to

$$\Delta L a 2\pi w_x = 4\pi a_m^2 u_0. \tag{32}$$

Set $\sqrt{2}a_m$ equal to $\sqrt{\Delta L a}$; then, $w_x=u_0$. The corresponding spherically symmetric radiated field of the monopole is

$$u_R = u_0 \frac{h_1^{(2)}[k_\alpha R]}{h_1^{(2)}[k_\alpha a_m]} e^{j\omega t}, \tag{33}$$

where $h_1^{(2)}$ denotes a spherical Hankel function for outgoing waves, R denotes the distance from the monopole location to the point of measurement, and k_α denotes the complex wave number for compression wave motion in the viscoelastic phantom material.[30] The vertical response at the free surface of the gel phantom can then be approximated by summing the response to all of the monopoles used in the discretization, accounting for the angle that the outgoing spherical wave makes with the vertical direction.

2. Dipole approach

For this case, the tube response is discretized with axial resolution ΔL and, this time, azimuthal resolution $a\Delta\theta$. The radial displacement calculated at the center of a segment of the tube extending ΔL by $a\Delta\theta$ is denoted as $w_{x\theta}$, and that entire segment of the tube is approximated as having radial displacement $w_{x\theta}$. See Fig. 9. A finite dipole of radius a_d vibrating with amplitude u_0 displaces a volume $\pi a_d^2 u_0$ directly in front of it. This is equated to the volume displacement of the portion of the tube the dipole represents, which is given by $\Delta L a \Delta\theta w_{x\theta}$. If one takes $\sqrt{\pi a_d}=\sqrt{\Delta L a \Delta\theta}$, then $w_{x\theta}=u_0$. The dipole is positioned at the geometric center of the tube wall segment it represents, and its axis is oriented normal outward to that segment. The corresponding radiated field is

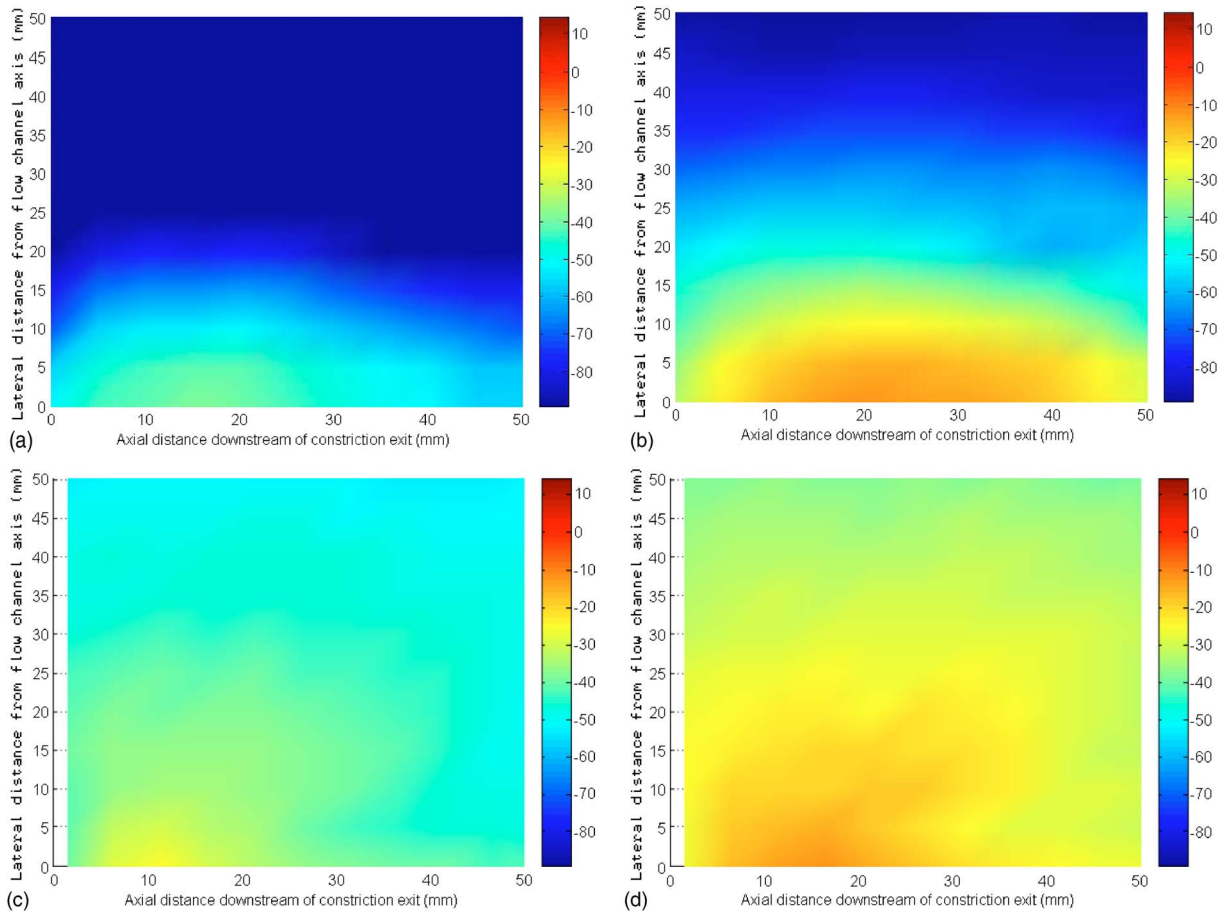

FIG. 13. (Color online) Vertical velocity (dB *re*: 1 mm/s) at phantom surface for constricted compliant tube embedded in soft tissue gel phantom as a function of axial and lateral position at 100 Hz. (a) Dipole theory, $\mathrm{Re}_D=1000$. (b) Dipole theory, $\mathrm{Re}_D=2000$. (c) Experiment, $\mathrm{Re}_D=1000$. (d) Experiment, $\mathrm{Re}_D=2000$. Online version uses color scale for dB.

$$u_R = N_1 \cos(\psi)\{[2 + 2jk_\alpha R - (k_\alpha R)^2]e^{-jk_\alpha R} + 2N_2(-jk_\beta R - 1)e^{-jk_\beta R}\}e^{j\omega t}/R^3, \tag{34}$$

$$u_\psi = -N_1 \sin(\psi)\{(-jk_\alpha R - 1)e^{-jk_\alpha R} + N_2[1 + jk_\beta R - (k_\beta R)^2]e^{-jk_\beta R}\}e^{j\omega t}/R^3, \tag{35}$$

where in this expression ψ denotes the angle made between the principle axis of that particular dipole and a vector drawn from the dipole to the point of measurement.[30] Here, R denotes the distance from the dipole location to the point of measurement, u_R and u_ψ denote the radial and tangential components of the generated vibratory field relative to the dipole, and k_α and k_β denote the complex wave number of the radiated compression and shear waves, respectively. Note that only dipole and measurement point combinations for which $-\pi/2 < \psi < \pi/2$ are used in the summation; i.e., only the field radiating radially outward from the vessel wall is used. The coefficients N_1 and N_2 can be specified based on the boundary conditions for "welded" contact or "lossless slip" contact. The welded contact case results in

$$N_1 = -u_0 a^3 e^{jk_\alpha a} \times \frac{3 + 3jk_\beta a - (k_\beta a)^2}{(1 + jk_\beta a)(k_\alpha a)^2 + 2(1 + jk_\alpha a)(k_\beta a)^2 - (k_\alpha a)^2(k_\beta a)^2}, \tag{36}$$

$$N_2 = e^{-j(k_\alpha - k_\beta)a}\frac{3 + 3jk_\alpha a - (k_\alpha a)^2}{3 + 3jk_\beta a - (k_\beta a)^2}. \tag{37}$$

The vertical response at the free surface is then approximated by summing the response to all of the dipoles used in the discretization, taking into account the angle that u_R and u_ψ make with the vertical direction.

B. Theoretical predictions and experimental measurements

Based on the approaches described above, the radial velocity of the latex tube and the vertical velocity at the gel surface for the constricted vessel and geometry of Fig. 1 were calculated at points directly above the embedded vessel and at points lateral to the tube axis downstream of the constriction. These results are shown in Figs. 10–13. The theoretical predictions in Figs. 11–13 were based on using sets of eight dipoles equally spaced circumferentially and axially

spaced at 2.5 mm to approximate the tube of length $L = 100$ mm. Increasing the dipole resolution further did not noticeably alter the results. Predictions using the dipole approach matched experimental measurements to a greater degree than those using the monopole approach; results based on the monopole approach are not shown. It is believed that this is due to the inability of the monopole approach to generate shear waves. Generally, it was observed experimentally that the overall vibration levels were greater than predicted via the dipole approach. This is believed to be partially due to the finite volume of the viscoelastic phantom resulting in multiple reflections, which the half-space theory does not capture.

In comparing Figs. 10(a)–10(c), 11(c), and 11(d), note that the prediction of the latex radial wall velocity closely matches the measured radial wall velocity and the measured gel vertical surface velocity just above the vessel, as expected given the shallow depth of the vessel ($\sim$6.5 mm from the surface to the top of the latex tube). The dipole approximation provides a less accurate prediction [Figs. 11(a) and 11(b)], but still captures the trends in frequency and location. The dipole approximation also enables a prediction of surface motion not directly over the vessel, capturing experimental trends as shown in Figs. 12 and 13. Experimentally, and in the theoretical simulation, it is observed that the surrounding viscoelastic gel material substantially, though not completely, dampens the resonant properties of the water-filled latex tube, resulting in a more uniform spectral content epicentered just downstream of the constriction, yet still possessing substantial frequency content well through several hundred hertz.

VI. CONCLUSION

The vibration of a thin-walled cylindrical, compliant viscoelastic tube with internal flow and an axisymmetric constriction that results in turbulent fluid flow was studied theoretically and experimentally. The developed closed-form analytical model of the coupled fluid and structural system may provide a baseline for future, more comprehensive analyses, analytical and computational, that may improve upon some of the indicated shortcomings or extend the approach to more complex and realistic geometries and material properties. Additionally, the reported experimental study provides a unique and comprehensive set of measurements and associated discussion relevant to vascular dynamics and diagnostics.

Vibration of the tube was considered with internal fluid coupling only, and with coupling to internal flowing fluid and external stagnant fluid or external tissuelike viscoelastic material. The theoretical analysis included the adaptation of a model for turbulence in the internal fluid and its vibratory excitation of and interaction with the tube wall and surrounding fluid or viscoelastic medium. Analytical predictions compared favorably with experimental measurements. Reasons for identified discrepancies between theory and experiment were provided. It was hypothesized that the primary reasons for these discrepancies were that (1) the empirical turbulence model did not fully account for compliant tube vibration and how it alters the turbulent field, and (2) the linear structural model of the tube did not capture some of the apparent nonlinear phenomena that were highly dependent upon the mean pressure within the tube. Note, it did appear that, when the tube was embedded in the viscoelastic material, the added inertial and dissipative loading on the tube attenuated these sources of discrepancy.

Extension of the theoretical modeling approach to more realistic and complex geometries may require numerical adaptations to predict the resulting transitional or turbulent flow field and surrounding solid tissue vibration in this highly coupled system. However, the analytical model provided here could be used to validate numerical techniques. Additionally, the developed theory could be used to provide estimates of the dynamic forces *in vivo* that relate to pathology and may be difficult or impossible to measure directly, such as the dynamic stress levels created in a vascular wall due to turbulent flow. Also, it is envisioned that the developed theoretical and experimental techniques may be helpful in evaluating and improving medical diagnostic technologies that utilize audible frequency phenomena generated below the skin surface to provide diagnostic information as an acoustic image or in another form.

ACKNOWLEDGMENTS

The financial support of the National Institutes of Health (EB002511 and HL55296) and the Whitaker Foundation (BME RG 01-0198) are acknowledged.

[1] R. Y. Kanterman, T. M. Vesely, T. K. Pilgram, B. W. Guy, D. W. Windus, and D. Picus, "Dialysis access grafts: Anatomic location of venous stenosis and results of angioplasty," Radiology **195**, 135–139 (1995).
[2] M. F. Fillinger, E. R. Reinitz, R. A. Schwartz, D. E. Resetarits, A. M. Paskanik, D. Bruch, and C. E. Bredenberg, "Graft geometry and venous intimal-medial hyperplasia in arteriovenous loop grafts," J. Vasc. Surg. **11**, 556–566 (1990).
[3] F. Loth, P. F. Fischer, N. Arslan, C. D. Bertram, S. E. Lee, T. J. Royston, W. E. Shaalan, and H. S. Bassiouny, "Transitional flow at the venous anastomosis of an arteriovenous graft: Potential activation of the ERK1/2 mechanotransduction pathway," ASME J. Biomech. Eng. **125**, 49–61 (2003).
[4] S. W. Lee, F. Loth, T. J. Royston, P. F. Fischer, H. S. Bassiouny, and J. K. Grogan, "Flow induced vein wall vibration in an arteriovenous graft," J. Fluids Struct. (in press).
[5] R. S. Lees and C. F. Dewey, "Phonoangiography: A new noninvasive diagnostic method for studying arterial disease," Proc. Natl. Acad. Sci. U.S.A. **67**, 935–942 (1970).
[6] B. Kim and W. K. Corcoran, "Experimental measurement of turbulence spectra distal to stenosis," J. Biomech. **7**, 335–342 (1974).
[7] G. W. Duncan, J. O. Gruber, C. F. Dewey, Jr., G. S. Meyers, and R. S. Lees, "Evaluation of carotid stenosis by phonoangiography," N. Engl. J. Med. **293**, 1124–1128 (1975).
[8] R. Gupta, J. W. Miller, A. P. Yoganathan, F. E. Udwadia, and W. H. Corcoran, "Spectral analysis of arterial sounds: A noninvasive method of studying arterial disease," Med. Biol. Eng. **13**, 700–705 (1975).
[9] R. J. Tobin and I.-D. Chang, "Wall pressure spectra scaling downstream of stenosis in steady tube flow," J. Biomech. **9**, 633–640 (1976).
[10] J. J. Fredberg, "Origin and character of vascular murmurs: Model studies," J. Acoust. Soc. Am. **61**, 1077–1085 (1977).
[11] W. H. Pitts III and C. F. Dewey, Jr., "Spectral and temporal characteristics of post-stenotic turbulent wall pressure fluctuations," ASME J. Biomech. Eng. **101**, 89–95 (1979).
[12] J. Wang, B. Tie, W. Welkowitz, J. Semmlow, and J. Kostis, "Modeling sound generation in stenosed coronary arteries," IEEE Trans. Biomed. Eng. **37**, 1087–1094 (1990).
[13] Y. Kurokawa, S. Abiko, and K. Watanabe, "Noninvasive detection of in-

tracranial vascular lesions by recording blood flow sounds," Stroke **25**, 397–402 (1994).
[14]M. Akay, Y. Akay, W. Welowitz, J. L. Semmlow, and J. B. Kostis, "Application of adaptive filters to noninvasive acoustical detection of coronary occlusions before and after angioplasty," IEEE Trans. Biomed. Eng. **39**, 176–183 (1992).
[15]A. Akay, M. Akay, W. Welkowitz, S. Lewkowicz, and Y. Palti, "Dynamics of sounds caused by partially occluded femoral arteries in dogs," Ann. Biomed. Eng. **22**, 493–500 (1994).
[16]A. O. Borisyuk, "Noise field in the human chest due to turbulent flow in a larger blood vessel," Flow, Turbul. Combust. **61**, 269–284 (1999).
[17]H. A. Mansy, S. J. Hoxie, N. H. Patel, and R. H. Sandler, "Computerized analysis of auscultory sounds associated with vascular patency of hemodialysis access," Med. Biol. Eng. Comput. **43**, 56–62 (2005).
[18]N. L. Owsley and A. J. Hull, "Beamformed nearfield imaging of a simulated coronary artery containing a stenosis," IEEE Trans. Med. Imaging **17**, 900–909 (1998).
[19]C. E. Chassaing, S. D. Stearns, M. H. van Horn, and C. A. Ryden, "Noninvasive turbulent blood flow imaging system," United States Patent No. 6,278,890 issued 8/21/2001.
[20]M. I. Plett, K. W. Beach, B. Dunmire, K. G. Brown, J. F. Primozich, and E. Strandness, Jr., "*In vivo* ultrasonic measurement of tissue vibration at a stenosis: A case study," Ultrasound Med. Biol. **27**, 1049–1058 (2001).
[21]R. L. Kirkeeide, D. F. Young, and N. R. Cholvin, "Wall vibrations induced by flow through simulated stenoses in models and arteries," J. Biomech. **10**, 431–441 (1977).
[22]J. B. Grotberg and O. E. Jensen, "Biofluid mechanics in flexible tubes," Annu. Rev. Fluid Mech. **36**, 121–147 (2004).
[23]W. L. Keith and B. M. Abraham, "Effects of convection and decay of turbulence on the wall pressure wavenumber-frequency spectrum," J. Fluids Eng. **119**, 50–55 (1997).
[24]R. K. Jain, "Vibration of fluid-filled, orthotropic cylindrical shells," J. Sound Vib. **37**, 379–388 (1974).
[25]A. Leissa, *Vibration of Shells* (Acous. Soc. Amer., 1993).
[26]M. C. Junger and D. Feit, *Sound, Structures and Their Interaction* (Acous. Soc. Amer., 1993).
[27]C. R. Fuller, "The input mobility of an infinite circular cylindrical elastic shell filled with fluid," J. Sound Vib. **87**, 409–427 (1983).
[28]B. J. Brevart and C. R. Fuller, "Energy exchange between the coupled media of impulsively excited, fluid-filled, elastic cylinders," J. Sound Vib. **190**, 763–774 (1996).
[29]X. M. Zhang, M. Fatemi, R. R. Kinnick, and J. F. Greenleaf, "Noncontact ultrasound stimulated optical vibrometry study of coupled vibration of arterial tubes in fluids," J. Acoust. Soc. Am. **113**, 1249–1257 (2003).
[30]T. J. Royston, Y. Yazicioglu, and F. Loth, "Surface response of a viscoelastic medium to subsurface acoustic sources with application to medical diagnosis," J. Acoust. Soc. Am. **113**, 1109–1121 (2003).
[31]T. J. Royston, H. A. Mansy, and R. H. Sandler, "Excitation and propagation of surface waves on a viscoelastic half-space with application to medical diagnosis," J. Acoust. Soc. Am. **106**, 3678–3686 (1999).